ASME Journal of Micro- and Nano-Manufacturing
Online journal at:
https://asmedigitalcollection.asme.org/micronanomanufacturing

Data-Efficient Surrogate Model for Rapid Prediction of Temperature Evolution in a Microscale Selective Laser Sintering System

Joshua Grose[1]
Department of Mechanical Engineering,
University of Texas at Austin,
204 E. Dean Keeton St.,
Austin, TX 78712
e-mail: joshgrose@utexas.edu

Aaron Liao
Department of Mechanical Engineering,
University of Texas at Austin,
204 E. Dean Keeton St.,
Austin, TX 78712
e-mail: aliao@utexas.edu

Chee Seng Foong
NXP Semiconductors,
6501 W. William Cannon Dr.,
Austin, TX 78735
e-mail: cs.foong@nxp.com

Michael Cullinan
Department of Mechanical Engineering,
University of Texas at Austin,
204 E. Dean Keeton St.,
Austin, TX 78712
e-mail: michael.cullinan@austin.utexas.edu

Current metal additive manufacturing (AM) systems suffer from limitations on the minimum feature sizes they can produce during part formation. The microscale selective laser sintering (μ-SLS) system addresses this drawback by enabling the production of parts with minimum feature resolutions of the order of a single micrometer. However, the production of microscale parts is challenging due to unwanted heat conduction within the nanoparticle powder bed. As a result, finite element (FE) thermal models have been developed to predict the evolution of temperature within the particle bed during laser sintering. These thermal models are not only computationally expensive but also must be integrated into an iterative model-based control framework to optimize the digital mask used to control the distribution of laser power. These limitations necessitate the development of a machine learning (ML) surrogate model to quickly and accurately predict the temperature evolution within the μ-SLS particle bed using minimal training data. The regression model presented in this work uses an "Element-by-Element" approach, where models are trained on individual finite elements to learn the relationship between thermal conditions experienced by each element at a given time-step and the element's temperature at the next time-step. An existing bed-scale FE thermal model of the μ-SLS system is used to generate element-by-element tabular training data for the ML model. A data-efficient artificial neural network (NN) is then trained to predict the temperature evolution of a 2D powder-bed over a 2 s sintering window with high accuracy. [DOI: 10.1115/1.4064106]

Introduction

Existing additive manufacturing (AM) technologies are limited by minimum feature resolutions of the order of hundreds of micrometers. This prevents the successful application of AM to several critical manufacturing domains [1,2]. The microscale selective laser sintering (μ-SLS) system addresses this problem through the production of metal parts with single micrometer feature sizes [3–6]. The μ-SLS machine is a specialized version of selective laser sintering (SLS), where laser energy is applied to a powdered substance to enable part formation through selective heating. This process is repeated layer-by-layer until a full 3D part is produced [7]. The key difference between μ-SLS and traditional SLS systems is the use of copper and silver nanoparticles instead of traditional macroscale powders. The small size of these metal nanoparticles enables the production of parts with the desired minimum feature resolutions. These nanoparticles do not melt and solidify like their macroscale counterparts. They instead experience solid-state diffusion at temperatures well below the melting points of the bulk materials. This diffusion process facilitates the production of microscale parts using the μ-SLS system.

To produce single micrometer features using the μ-SLS system, thermal modeling techniques are required to predict and minimize the formation of unwanted heat affected zones (regions of sintering in the particle bed that extend beyond the desired part shape). These heat affected zones form in response to laser heating and subsequent rapid conduction within the particle bed. A bed-scale finite element (FE) thermal model is developed for the μ-SLS system to predict this heat spread in the particle bed and determine the resulting temperature evolution during the sintering process [8]. Ideally, this thermal model would integrate into an iterative control framework used to optimize the μ-SLS system parameters and improve the feature resolution of printed parts. The major limitation of this integration strategy is the extensive computation times required to execute high fidelity thermal FE models. A much faster thermal model is required to efficiently control heat spread and optimize sintering performance.

Surrogate models are often used as fast and accurate replacements to classical models when computational expense is a constraint. For instance, a high-fidelity sampling approach was used to achieve accurate predictions of physics-based processes with minimal training data. The surrogate model Brain-STORM was deployed using deep learning-based strategies for rapid prediction of the

[1]Corresponding author.

Contributed by the Manufacturing Engineering Division of ASME for publication in the Journal of Micro- and Nano-Manufacturing. Manuscript received July 10, 2023; final manuscript received November 6, 2023; published online January 10, 2024. Assoc. Editor: Shih-Chi Chen.

transient evolution of smoke flow, pressure, and temperature during high-rise fire scenarios. Brain-STORM is trained on data produced by Fire-STORM, a previously developed physics-based model [9]. Tapia et al. developed a cross-validated, computationally efficient Gaussian process based surrogate model trained on a high-fidelity laser powder bed fusion model. This model showed good performance demonstrated by a low mean absolute predictive error [10]. These models demonstrate the ability of surrogate models to act in place of existing, computationally expensive models while maintaining useful predictive capacity.

Surrogate models have also been proposed as approximators for finite element analysis (FEA) and finite volume modeling to reduce computational complexity. These models are trained on input/output data generated by the FE models. These surrogate models perform well in a variety of tasks including prediction and sensitivity analysis [11]. FEA based surrogate models have been used in biomechanical applications to reduce the simulation time of anatomical simulations, improving their usability for clinical applications [12]. Additionally, Liang et al. developed a feedforward fully connected neural network with four hidden layers as an inverse method to successfully estimate and recover the human thoracic aorta zero pressure geometry [13]. Vurtur Badarinath et al. estimated the stress distribution over a one-dimensional beam using machine learning surrogate models, where FEA data represented response variables such as displacement, velocity, acceleration, strain or stress [14]. Masood et al. proposed a data driven design optimization process for a Kaplan turbine, incorporating a Gaussian process based surrogate model for efficient prediction [15]. Dupuis et al. proposed a methodology for prediction of steady turbulent aerodynamic fields while handling variable flow conditions [16]. This model provided improved accuracy when compared to existing surrogates capable of handling diverse flow regimes. Sikirica et al. developed machine learning (ML) based surrogate models for heat transfer calculation to optimize microchannel heat sinks [17]. Neural network (NN) architectures were compared with random forests and gradient boosting algorithms for performance. Compact long short-term memory networks have previously been proposed to predict responses as an alternative to finite element simulation data when time dependent predictions are required [18]. Bottlenecks for the accuracy of a machine learning surrogate model trained on finite element data include limited mesh sizes and fixed input parameters. However, if the generated data captures the essential use cases, the model will still be useful in practice.

Additionally, FE base surrogate models have been employed as computationally efficient alternatives to high-fidelity models for additive manufacturing applications. Surrogate models have been shown to have enormous potential for computational gains when compared to baseline physics-based models, enabling advancements in the optimization of additive manufacturing processes [19]. Wang et al. constructed a surrogate model capable of predicting the three-dimensional melt pool geometry formed during metal AM fabrication and estimated the associated uncertainty. The validity of the surrogate model was then improved using sequential Bayesian calibration [20]. Despite the successful modeling results accomplished in other works, no present surrogate model can predict the nuanced, nanoparticle heat transfer processes that occurs within the μ-SLS system.

Heat transfer based ML models have gained popularity as surrogates for temperature field prediction and heat source layout (HSL) optimization for integrated circuit applications. Zhao et al. developed a deep convolutional image-to-image regression model for rapid prediction of temperature fields for given HSLs [21]. This model employs temperature field difference based data augmentation, transfer learning, and a feature pyramid network for improved performance in the presence of limited data for data hungry convolutional neural network (CNN) architectures. Chen et al. built a similar model based on the feature pyramid network architecture for thermal optimization of HSL [22]. A multimodal neighborhood search algorithm is used to avoid convergence on local optimum during HSL optimization. Yang et al. used a U-net CNN architecture to predict the temperature field in a two-phase composite under a given HSL. Each of these HSL thermal surrogates use CNN-based architectures to predict thermal images as functions of input energy distribution images (HSLs) [23]. While the HSLs are similar to the digital laser masks used to control heat generation in the μ-SLS system, these models only predict and update temperature values. They are not suitable for the multivariable prediction of temperature and densification needed for part prediction in the μ-SLS system. The surrogate model developed in this work must predict the entire temperature field over time while simultaneously updating the densification as a function of the developing temperature. This requirement makes it difficult to use similar strategies for μ-SLS surrogate model development.

Modern advancements in ML have prompted the development of advanced surrogate models using novel neural network architectures including modern CNN architectures and graph neural networks [24,25]. These models have shown the ability to achieve very high accuracy for a variety of physics-based applications while maintaining rapid computational times. Unfortunately, these models require large training datasets consisting of hundreds or thousands of simulations. Given that the μ-SLS system is currently in an iterative development stage, the underlying bed-scale finite element model used to generate the training data is subject to change. This promotes the need for a surrogate model capable of providing accurate predictions after training on a smaller simulated dataset. This surrogate model must also be robust to changes in the underlying FE model during system development.

This paper presents a surrogate modeling approach for rapid temperature prediction over time in a μ-SLS particle bed. The handcrafted features implemented in the model provide direct information regarding the thermal conditions present in the system, allowing for high accuracy when trained on minimal data. This model can out-perform the long computation times experienced by classical simulations that discretize and solve the heat equation. This facilitates the implementation of a mask optimization process that requires iterative prediction and mask adjustment. The improved computational speed provided by the surrogate model is needed to perform the large number of computations required for this mask optimization process.

Methods

Sufficient data detailing the transient evolution of the μ-SLS particle bed in response to laser exposure is needed for an ML based surrogate model to accurately predict temperature changes in the system. This temperature data are generated by running a high-fidelity finite element model (FE model, FEM) with a series of unique input laser patterns. This work employs an element-by-element methodology, where ML predictions are made on individual elements in the FE mesh. As a result, specific features about each element within the particle bed and its surrounding elements are extracted from the FEM output data. Custom features are also incorporated that detail the spatial relationship between each element and the overall distribution of applied laser power. Finally, features detailing sudden changes in laser exposure are incorporated for more realistic use cases. Once features are extracted for each element in the mesh and a simulated dataset is formulated, an artificial NN is trained to predict temperature evolution of a single element based on each of its extracted features.

Finite Element Model Data Generation. A bed-scale thermal FE model is used to generate temperature, density, and volumetric heat generation (Q_{gen}) data for a single layer particle bed exposed to laser irradiation over a 2 s sintering window. The bed-scale model simulates a thin layer of copper particles (1.2 μm in thickness) resting on a thick glass substrate (1 mm in thickness). The thin copper bed is split into two regions: a rectangular inner mesh region in the immediate vicinity of the laser exposure region (1.5 mm $\times$ 3 mm), and an outer rectangular meshing region (4 mm $\times$ 6 mm) that surrounds the inner region. These two copper

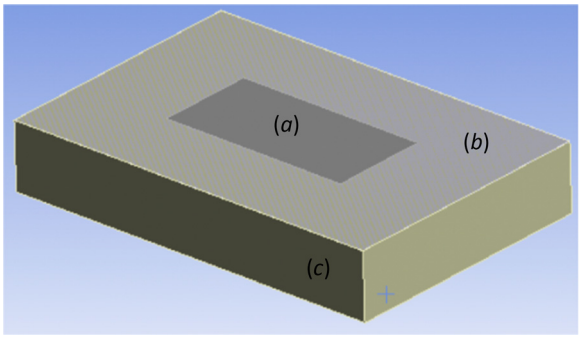

Fig. 1 Physical geometry used in FEA simulations, with (*a*) representing the inner copper region (fine mesh), (*b*) representing the outer copper region (coarse mesh), and (*c*) representing the glass substrate

regions are the same thickness, sit at the same z-location and are in perfect thermal contact with each other. The inner copper region is used for data generation, and the outer region is used to decouple boundary effects from the resulting temperature distribution. The split regions allow for accurate modeling of the powder bed while maintaining a reasonable quantity of output training data. The full model geometry is shown in Fig. 1.

The inner region of the thin copper bed is exposed to laser irradiation in select regions of the particle bed determined by a projected binary image mask. An example binary mask is shown in Fig. 2.

This digital mask is the same mask that is applied to the digital micromirror device (DMD), a mirror array used by the physical μ-SLS system to control the distribution of applied laser power. White pixels in the mask transmit the maximum laser power at the corresponding location, while black pixels restrict all laser power transmission. Laser irradiation passing through the DMD also passes through a downstream optical system before reaching the copper bed. The 1920×1080 pixel binary image can expose a 2.3 mm $\times$ 1.3 mm region when the binary mask consists exclusively of white pixels. The binary mask is projected onto the simulated inner copper region using the same magnification used in the μ-SLS optical system. A series of unique and intricate part shapes can be fabricated simply by replacing this digital mask. In the simulation, the binary mask induces heat generation in the same locations as in the physical system. Each element in the FE mesh is mapped to a projected binary mask pixel. Elements corresponding to white pixels produce the maximum value of generated heat, while elements corresponding to a black pixel do not generate heat.

The particle bed used in the physical μ-SLS system undergoes substantial changes in particle morphology during sintering, and thus cannot be accurately represented by a uniform copper block. To address this, the FE model is integrated with property functions that

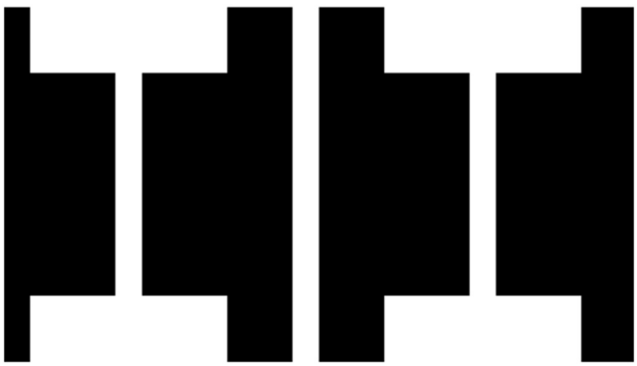

Fig. 2 Simple "double-I" binary mask (1920 × 1080 pixel count) used to control DMD mirrors and selective application of laser power

model the evolution of thermal properties within the powder bed as the morphology of the particles change during sintering. As copper particles reach the 450 °C sintering threshold they begin to experience diffusion between adjacent particles, forming necks between particles and increasing the density of the sintering regions over time. The necks that form between particles become larger as diffusion occurs, providing larger pathways for heat to pass through within the sintering region. These larger pathways result in thermal conductivity values that increase proportionally with density.

In the simulation, values for density and thermal conductivity for each element are updated at ten specified timesteps over the 2 s simulation window (every 0.2 s of simulation time) based on the element temperatures at the specified timesteps. This coarse property update frequency reduces the time spent updating material properties at the cost of sudden redistributions of temperature in response to material property changes. The surrogate model will update with a much finer frequency to improve accuracy of the temperature results when used in practice. Simulated sintering for each element in the FE mesh begins once the element temperature exceeds 450 °C at any of the specified timesteps when property updates occur. Once elements begin to sinter, their individual densities and thermal conductivities are updated according to the property relationships developed in Refs. [26] and [27]. The FE simulation is initialized at room temperature, with all elements set to 22 °C. The bottom surface of the glass substrate is held at 22 °C for the duration of the simulation. Convection and radiation are not considered in the FE model, as the contributions of both are negligible when compared to heat conduction at the microscale. Contributions of convection and radiation were tested empirically during model development, and as a result all additional faces were insulated. Additional information regarding the thermal property update procedure used in the FE model is discussed in Ref. [8].

When generating the data, the size, and shape of the mesh elements in the FEM are fixed. 20 node hexahedral elements are used throughout the copper bed, with a fine mesh size of 2.5×10^{-5} m applied to the inner region and a larger mesh size of 1.0×10^{-4} m applied to the outer region. The size and shape of the copper bed and glass substrate are also fixed. These constant parameters accurately represent the physical system, while limiting the variation in training data. A constant absorbed laser power of 3.55×10^6 W/m^2 is used for regions exposed to the laser via the digital laser mask. While this laser power is slightly higher than laser powers used in the physical system, the accuracy of the surrogate model when predicting reduced laser powers is comparable to the results presented in this work. For the initial training dataset, three unique masks are used to control laser application during three separate simulations. Each of the three input masks determined the distribution of laser power for its corresponding simulation, and this power distribution remained constant throughout the sintering window. At the end of each simulation, temperatures at 133 timesteps over a 2 s window are saved for each node in the system.

Density, thermal conductivity, and normalized Q_{gen} values are updated for each element at ten specified timesteps over the 2 s window, resulting in ten unique density and Q_{gen} values for each element. Q_{gen} values are determined based on the given element's location relative to the 2.3×1.3 mm^2 exposure region that corresponds to the selected mask after projection through the focusing optical system. $Q_{\text{gen}} = 1$ if the element is exposed to a white pixel and $Q_{\text{gen}} = 0$ if the element is exposed to a black pixel. Density values are determined from the nanoparticle property curves developed in Ref. [26]. After each simulation, constant value interpolation is used to expand the ten Q_{gen} and ten density values for each element to match the full 133 time-step nodal dataset. Since the temperature time series is saved for each node, and the Q_{gen} and density values are saved for each element, nodal temperatures must be mapped to element temperatures to maintain a uniform data shape. Since each hexahedral element consists of 20 associated nodes, each of the 20 nodal temperatures associated with a particular element are uniformly averaged to obtain the temperature of the element. This process is repeated for every element at every time-

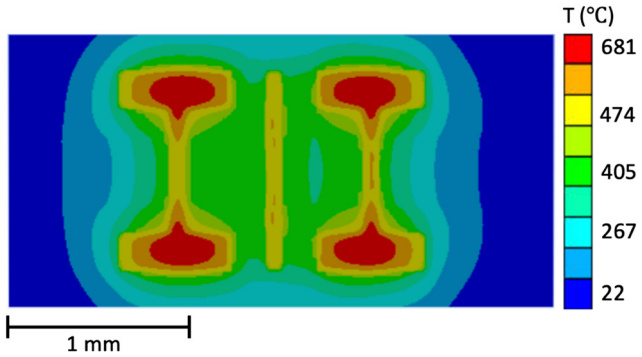

Fig. 3 Temperature distribution across the inner copper region at final time-step as predicted by the ANSYS FE model using the "double-I" mask

step. The final exported dataset corresponding to each of the three simulations includes 7080 elements in a 60 × 118 element grid, with each element represented by Q_{gen}, density and temperature values for each of the 133 simulation timesteps. The updated thermal conductivity values are not included in the dataset given that thermal conductivity is a direct function of density. The temperature values corresponding to each element at the final time-step of the training data (as generated by the FE model using the "double-I" mask) are shown in Fig. 3.

Feature Extraction (Single Mask). The objective of the ML model is to predict an element's temperature at a subsequent time-step based on features of the element at the current time-step. For this regression model, the training label for an individual element is the subsequent temperature of the element at the next time-step. This prediction process is performed for all elements in the inner copper region and repeats for each time-step as the model walks through and predicts the full timeseries. The training features that form the input dataset are described in detail in this section.

Explicit Finite Element Analysis Features: Elements and Surroundings. The first features extracted from the FE model results for a given element are as follows: element temperature, element volumetric heat generation (Q_{gen}), and element density at the current time-step. The next set of extracted features are the temperature, volumetric heat generation (Q_{gen}), and density values for the eight elements directly surrounding the specified element. These features capture the state of the specified element, in addition to the state of the element's immediate surroundings, giving context regarding the local distribution of energy and temperature around the element. This feature subset includes 27 total features (three features for the current element and 24 features for the surrounding elements). An illustration of the elements incorporated into this feature subset is shown in Fig. 4.

Derived Features: Spatial Energy Distribution. An initial model was trained only on the explicit FEA features, and the resulting accuracy was poor. Temperature gradients were limited to the region immediately surrounding the portion of the bed that was exposed to laser power, proving that the ML model was unable to adequately learn heat transfer within the bed. Expanding the set of surrounding element features had minimal impact on the prediction accuracy. To account for this spatial inaccuracy, two new feature types were added to the model that consider the spatial arrangement of exposed elements relative to the selected element. The first set of these features, labeled the "Q_{gen} zones," count the number of exposed elements in expanding ring-shaped regions around the selected element. This feature helps capture the element's proximity to large sources of heat generation. The number and size of each Q_{gen} zone were set as parameters for model tuning. The final model used six Q_{gen} zones for each element, with zone thickness increasing with each subsequent zone moving radially away from the selected

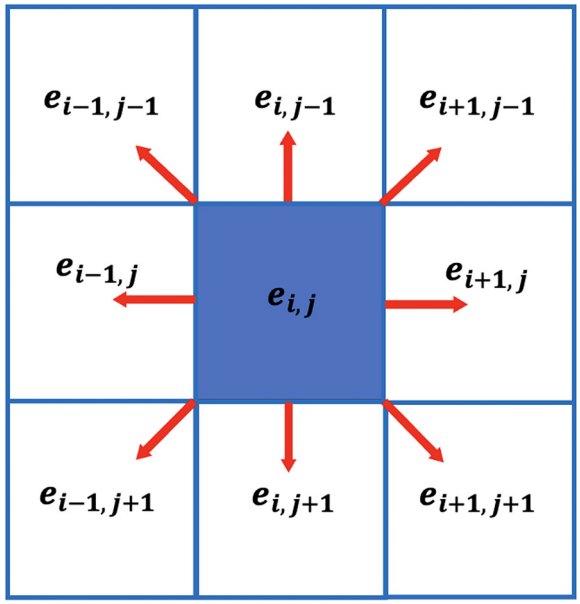

Fig. 4 Illustration of specified element on which the surrogate model will predict temperature and its surrounding elements. Each element contributes temperature, density, and Q_{gen} to the training dataset. Adjacent elements are labeled with position indices relative to the target element.

element. An illustration of the first three Q_{gen} zones for an example element is shown in Fig. 5.

The introduction of the Q_{gen} zone features greatly improved the model accuracy when predicting the spatial temperature distribution at each time-step. Despite this improvement, the limited range of the Q_{gen} zones failed to adequately account for the heat generated by the full set of exposed elements. To further improve the model, a new feature representing the global energy distribution was added to supplement the Q_{gen} zones. This feature, labeled "Q_{gen} distance," encodes information about the entire digital mask for each specified element in the mesh. The value of Q_{gen} distance for each element was calculated using the following equation:

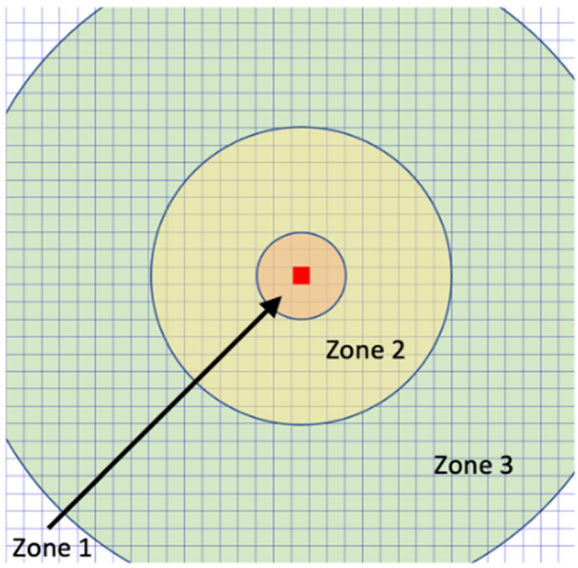

Fig. 5 Illustration of three of the six Q_{gen} zone features for an example element (shown in the center). Moving radially outward, each Q_{gen} zone is larger than the preceding one. Six Q_{gen} zones are attributed to each element. Each zone counts the total number of exposed elements (Q_{gen} = 1) that have centroids located in the zone.

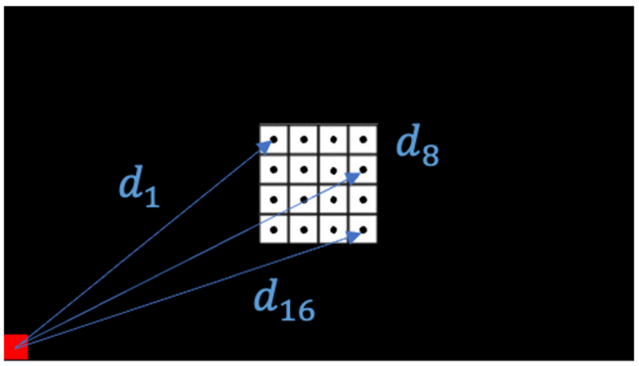

Fig. 6 Illustration of the distance parameters used in the Q_{gen} distance feature calculation for a single element located in the bottom left corner of the sintering region. White squares represent elements exposed to laser irradiation. The Q_{gen} distance feature calculates the distance between the specified element (red) and each exposed element (white) and then performs the calculation shown in Eq. (1). Elements shown in black are not exposed, and therefor do not contribute to this feature (Q_n=0). Only three of the 16 distance values are shown for simplicity. The displayed mesh is coarser than the one used in this work.

$$Q_{\text{gen}}\ \text{distance} = \sum_{n=1}^{7079}\left(\frac{Q_n}{d_n^{1.2}}\right) \tag{1}$$

where n represents the index of another element in the mesh (1–7079), Q_n represents the heat generation experienced by the indexed element, and $d_n^{1.2}$ represents the Euclidean distance between the specified element and the other element in the mesh. This ratio of laser power to distance between elements was summed over all mesh elements excluding the specified element. Elements with a Q_{gen} value of 0 (unexposed) did not contribute to this feature. Likewise, exposed elements closer to the specified element (smaller $d_n^{1.2}$) will have a greater impact than elements farther away (larger $d_n^{1.2}$). The full summation process over the 7079 other elements is performed for each specified element in the mesh. The Q_{gen} distance feature provided explicit information regarding the spatial energy distribution across the entire bed for each specified element. The exponent of 1.2 on the distance parameter was chosen after testing the performance of models trained on different values in the range of 0.8–1.5. The addition of the Q_{gen} distance feature significantly improved the model's ability to capture spatial temperature distributions across all model tests. A diagram of the distance values used for this feature is shown in Fig. 6.

In total, the training dataset for the best performing model included 27 explicit features and seven derived features for a total of 34 features for each specified element. The feature set for each of the three digital masks were combined to form the full training dataset, consisting of 2,824,920 training points (7080 elements, 133 timesteps, three masks).

Feature Extraction (Mask Vector). The training dataset consisting of 34 features and three FE simulations represents the system's thermal response to a constant distribution of laser power (a single mask is applied for the full 2 s sintering window). The thermal surrogate model developed in this work will be integrated into a model-based control framework capable of optimizing the digital mask at specified timesteps during the sintering window. This optimization process will produce a series of unique masks (one at each specified update step), forming a vector of digital masks. Therefore, the surrogate model developed in this work must be able to adapt to sudden changes in the laser power distribution to accurately model thermal evolution in realistic scenarios. New features and additional training data are added to the model in cases where the model must adapt to these changes in laser power.

Data driven surrogate models can only learn relationships present in the available training data. The training data produced by the three FE simulations did not include situations where sudden mask changes occurred during runtime. As a result, additional training data representing these mask changes were supplied to an expanded training dataset. A total of six additional simulations were added to the dataset, resulting in nine total simulations. This set of six additional simulations consisted of two subsets, each containing three new simulation datasets. Simulations in the first subset were run exactly as the initial single mask simulations were, with exception of the laser mask input. The single masks used in the original simulations were replaced with a mask vector containing three different masks. Each of these three masks were run for 1/3 of the 2 s sintering window, with each subsequent mask having a smaller exposure region than the previous mask. Although the exposure regions reduce in size during the simulation, the shape displayed in the mask remains the same. An example mask vector in this first subset is shown in Fig. 7.

The second subset of additional simulations used the same set of masks as the first subset, but with the mask vector organized in the opposite order. These mask vectors also consisted of masks with the same base shape, but with each subsequent mask gradually increasing the size of the laser exposure region during the sintering window. As before, each of these three masks were run for 1/3 of the 2 s sintering window. An example mask vector from this second group of additional masks is shown in Fig. 8.

In addition to the expanded training dataset, an additional feature was added to the feature set to capture the sudden change in applied laser power. The initial models that were trained on the expanded dataset failed to capture the rapid temperature changes that correspond to a sudden adjustment to the distribution of laser power. To account for this, a new feature was added to explicitly instruct the NN to adjust the temperature predictions in response to a sudden mask change. For a given element, this new feature determines the difference between the smallest Q_{gen} zone feature at the current time-step (after the mask change), and the smallest Q_{gen} zone feature from the previous time-step (before the mask change). This calculated difference represents the change in laser energy experienced by an individual element at the time of a sudden change in the digital mask. This encodes information regarding the sudden redistribution of laser power experienced by the mask into a

Fig. 7 Example mask vector with "vanishing" exposure region used to generate mask change training data

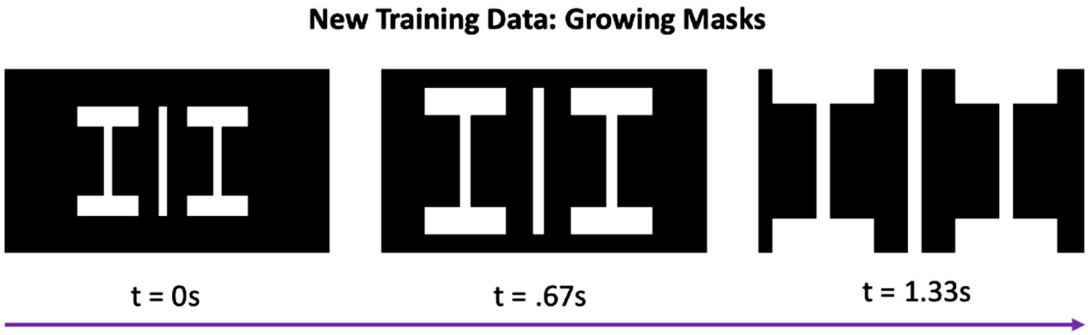

Fig. 8 Example mask vector with "growing" exposure region used to generate mask change training data

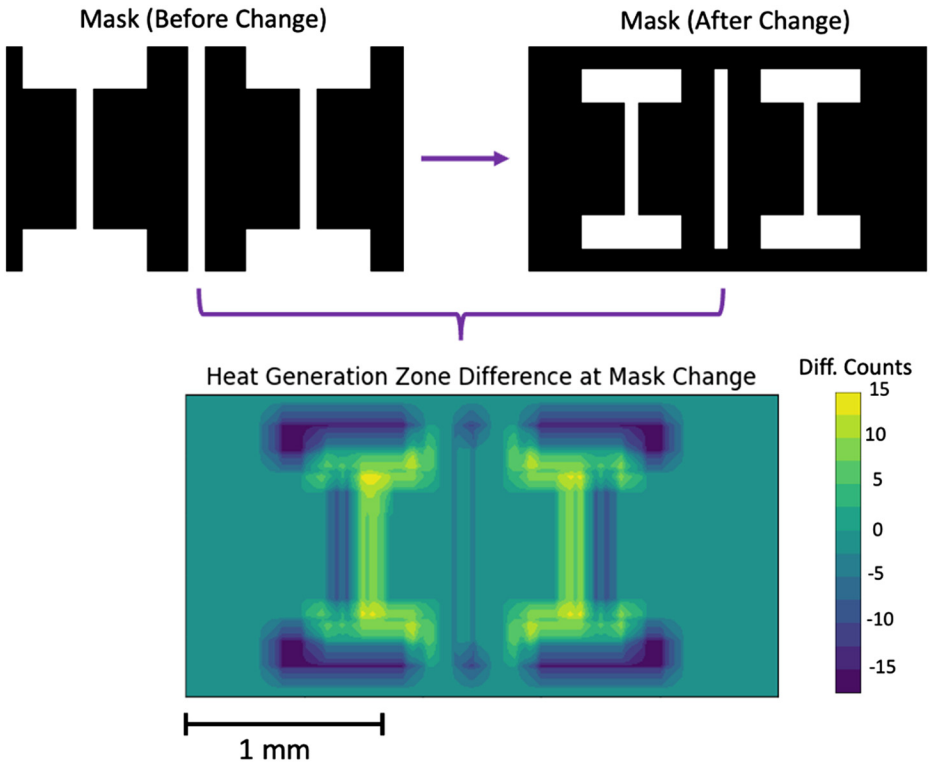

Fig. 9 Example training feature representing the change in laser exposure experienced by each element in response to the change in digital mask

training feature. This feature value is zero for all timesteps, where the mask does not change, is negative for an element that experiences a reduction in laser exposure and is positive for an element that experiences an increase in laser exposure. The use of the smallest Q_{gen} zone in place of the raw Q_{gen} value at each timestep gives a broader picture of the energy change experienced by an element during the mask change. An example image depicting this feature for the entire mesh is shown in Fig. 9.

The new training dataset consisted of 8,474,760 training points (7080 elements, 133 timesteps, nine masks). The incorporation of additional training data and the mask change feature greatly improved the ability of the model to predict temperature evolution in response to a variable mask vector.

Model Selection. Once tabular data was generated, three modeling frameworks were considered as surrogate candidates: a five layer fully connected NN (three hidden layers), extreme gradient boosted decision trees (XGBoost), and a distributed gradient boosting framework (LightGBM). NNs are an appropriate choice as a surrogate model because of their ability to approximate any underlying functional relationship with computationally efficient prediction times. However, NNs require a large amount of time for hyperparameter optimization and model training. Next, XGBoost employs a predictive model based on an ensemble of weaker predictive models. XGBoost is known to avoid overfitting, predict in a computationally efficient manner, and generalize well. Additionally, LightGBM tends to have fast training speed, high efficiency, low memory usage, and better accuracy when compared to other boosting algorithms. Each of these models are capable of training on the tabular dataset and producing a regression model capable of predicting element temperature. However, the NN produced predictions with the lowest mean average error across the testing set. Additionally, the NN produced smooth temperature contours, in contrast with the jagged temperature curves predicted by the ensemble methods. Smooth temperature contours better represent the continuous temperature profiles present during sintering, and allow for estimation of smooth thermal gradients within the bed. For these reasons, the NN was selected as the model architecture for this work.

The final NN architecture consisted of five layers, with three hidden layers (each with 24 hidden nodes). The input layer contained

a number of nodes equal to the number of training features, and the output layer consisted of a single node (with a linear activation function) for the predicted temperature value. The Adam optimizer was chosen due to its fast convergence properties, which were especially valuable during iterative model development. After model training, the epoch with the lowest validation loss during training was chosen as the final model. The ELU, ReLU, and Leaky ReLU activation functions were tested for training time and model performance. The ReLU activation function was ultimately chosen for this work for the following reasons. The performance of models trained on ReLU is independent of the underlying distribution of the data, making ReLU considerably more versatile than other activation functions. These models also benefit considerably from reduced computational time during gradient calculation. Finally, models trained using the ReLU activation function saw the best performance despite similar training times during model testing. The entire ML model was developed in Python using the Tensorflow and Keras NN implementations.

Results and Discussion

The results section is split into six sections. The first section discusses the parameters chosen for the model and how the model is setup for prediction. The second section shows temperature results predicted by the trained NN for uniform laser masks. The third section details temperature predictions on more complicated mask vectors. The fourth section presents part prediction results derived from temperature prediction data. The fifth section compares the runtime between the surrogate model and the FEA model, and the final section describes the model validation process and future work.

Modeling Parameters and Prediction Setup. The five-layer NN was initially trained on the single-mask training dataset consisting of 2,824,920 training points, each with a label representing the temperature at the next time-step. The three masks used to generate the training dataset are shown in Fig. 10.

The three training masks were initially chosen to generate unique temperature distributions. Together, the three masks contain large, concentrated pixel groups, small "islands" of pixels, convex and concave corners, sharp edges, and smooth curves. Additionally, the three masks help generate a wide range of final element temperatures. Masks with these geometric features allow the model to learn a more comprehensive set of laser power distributions and element temperatures, improving the final model's ability to predict on a range of new mask inputs. Additional masks from the testing set were swapped for these training masks, but the resulting models suffered from reduced accuracy. The input layer of the NN consisted of 34 neurons to match the number of training features, each hidden layer of the NN consisted of 24 neurons each, and the output layer contained a single neuron for the predicted temperature of the specified element. The number of neurons in each of the hidden layers was determined empirically by performing a hyperparameter grid search. The ReLU activation function was used as the nonlinear activation function between layers. Mean squared error was selected as the loss function for training, and the Adam optimizer was chosen to minimize error. The training dataset, the feature set, and the number of input neurons were later adjusted to adapt the model to more complex mask vectors.

Neural Network Prediction Results (Single Mask). The trained NN was then used to predict thermal evolution in the nanoparticle bed for seven new input masks over the full two second sintering duration. These masks were chosen to represent unique shapes with substantially different laser power distributions for robust testing. The collection of testing masks is shown in Fig. 11.

The NN was trained for 20 epochs to predict the temperature of a single element at the next time-step given an input feature vector containing temperature and heat generation information at the current time-step. Training for additional epochs resulted in similar performance with longer training times. Once trained, the NN was used to predict the transient thermal evolution of the particle bed for seven test masks. The initial conditions used for the NN prediction match the conditions used in the FE model, with all elements initialized at room temperature at time-step 0. The laser exposure (Q_{gen}) for each element at the initial time-step is sampled directly from the chosen mask, as are the Q_{gen} values at subsequent timesteps. A constant mask is used for the entire 2 s simulation, so Q_{gen} for each element remains constant during simulation and prediction. Using element data from time-step 0, the NN is used to individually predict the temperatures for each element in the copper bed at time-step 1. Once the temperature of each element has been predicted at a subsequent time-step (using time-step 0 data to predict time-step 1 temperatures), the predicted values are converted back into the form of the original training data to predict the next time-step. Current and adjacent elements temperatures and Q_{gen} values are remapped into the training data format. Element density is recalculated every 0.2 s during prediction to match the property update frequency used in the FE model. Once the results have been reformatted, the NN again predicts the next time-step in the series. This process continues until the final time-step is reached, representing a completed 2 s sintering process. The temperature distributions from the FE model (true values) and the neural network predictions for two of the testing masks are shown in Fig. 12.

The temperature distributions in Fig. 12 directly compare the NN predictions to the original FEA results. The data generated using the testing masks are independent of the data used in training. The first image in each figure shows the binary masks used to control laser power for each comparison. The second image depicts the final temperature distribution predicted by the NN, the image directly below it shows the temperature distribution predicted by the FE model, and the final image shows the percentage error between the two predictions for all elements after 2 s of sintering. The overall shape and magnitude of the NN predicted temperature plots agree very well with the FEA data. The NN accuracy is also consistent across the seven masks tested. An overall mean average error for all elements used in all seven test simulations was calculated to be 12 °C, with a mean average percentage error (MAPE) of 5.5%. These error values are calculated after 133 consecutive predictions over the full timeseries, where error accumulates after each subsequent prediction.

The temperature evolution of the element located at the center of the simulation bed is shown for the same two test masks in Figs. 13 and 14.

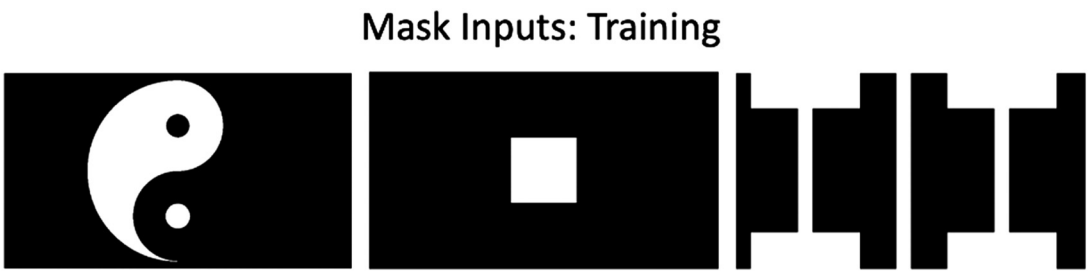

Fig. 10 Binary masks used as input to generate training data for the ML model

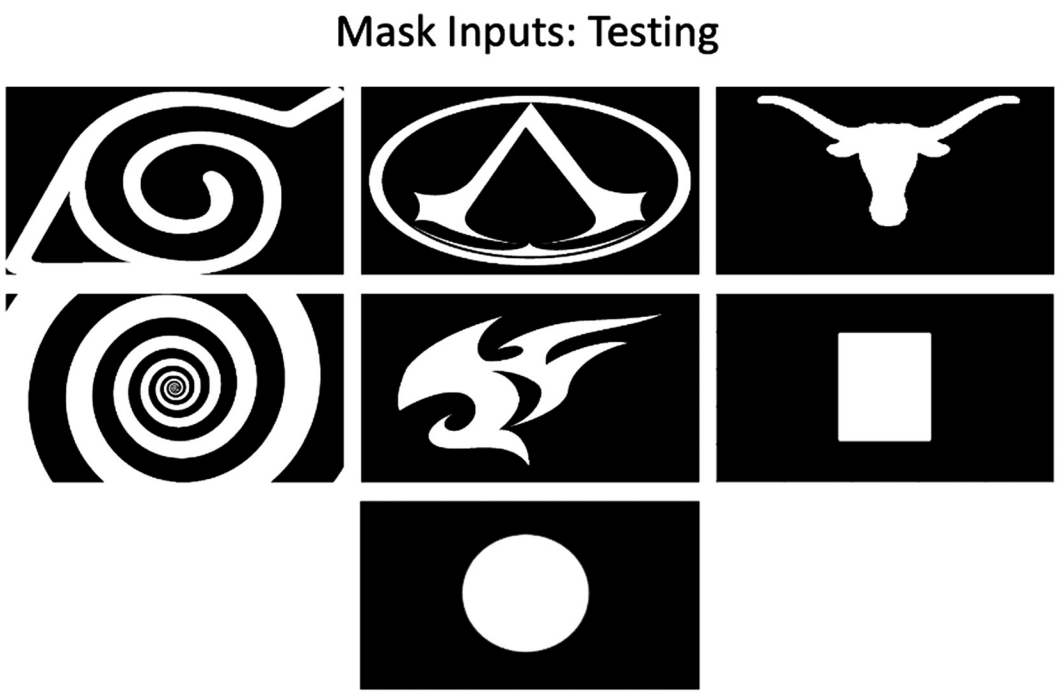

Fig. 11 Binary masks used as input to generate testing data for model evaluation

The overall temperature trajectory predicted by the NN matches well with the FEA results. The NN accurately predicts the initial rapid heating and the asymptotic behavior experienced by an element as it approaches thermal equilibrium. The coarse update frequency used to modify the thermal properties of the particle bed results in sudden changes in temperature at each update time-step. Future simulations will increase this update frequency to better model the continuous property changes that occur during sintering.

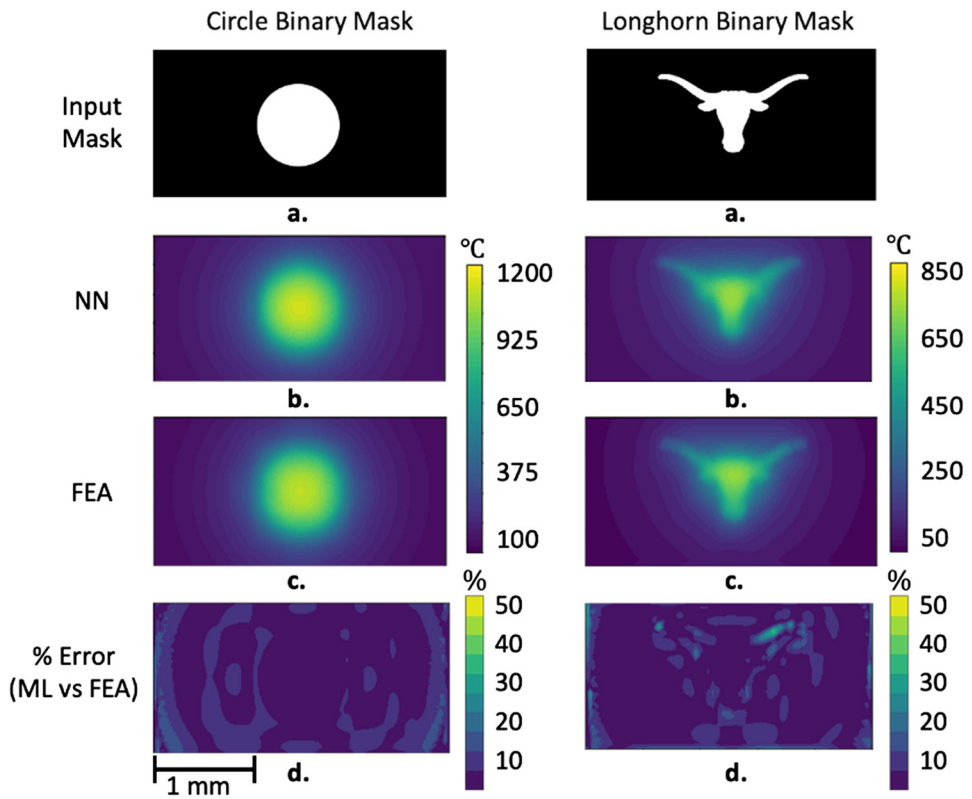

Fig. 12 Full 2D temperature profiles after 2 s of sintering (133 consecutive predictions: (*a*) binary masks used as simulation inputs, (*b*) temperature profiles generated by the NN for the circle mask and longhorn mask, (*c*) temperature profiles generated by the FE model for the same masks, and (*d*) the percent error between the two predictions at each element. Avg. error: 3.86% (circle), 3.64% (longhorn).

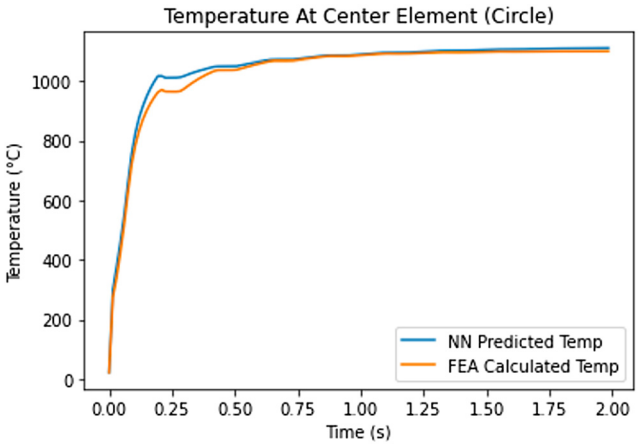

Fig. 13 Center element temperature over time (ML versus FEA) using the circle mask

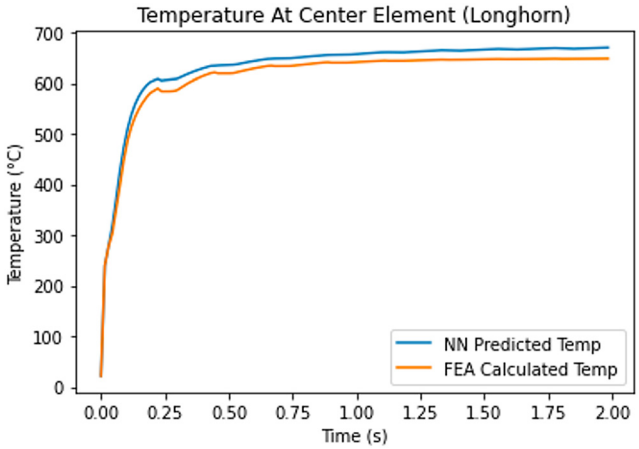

Fig. 14 Center element temperature over time (ML versus FEA) using the longhorn mask

The results in Figs. 13 and 14 illustrate the NN's ability to respond to these property changes and adjust temperature accordingly in a way that matches the FEA results. Temperature curves for other elements and other test masks also follow similar trends.

Neural Network Prediction Results (Mask Vector). The model setup used to predict temperature evolution in response to a variable mask vector was identical to the setup described for the single mask, with exception of the additional training data and the new mask change feature described previously. A custom mask vector consisting of three masks was used as testing data to evaluate the surrogate model's ability to accurately model sudden changes in laser power distribution. This mask vector contains three images of a longhorn, with each subsequent mask providing a scaled-down version of the pervious mask (subsequent masks have smaller exposure regions). This mask vector was not included in the training set. At the onset of the testing procedure, the initial mask was loaded exactly as the masks were loaded when predicting the results for single masks. Once the surrogate model predicted a series of temperature values over a predetermined set of timesteps, the initial mask was then replaced by the second mask in the mask vector. This process was repeated for each mask in the mask vector until the simulation terminated. The prediction results are shown at three simulation timesteps along with the corresponding mask vector in Fig. 15.

The results shown in Fig. 15 show the surrogate model's ability to accurately model the temperature evolution over a full sintering window with changing laser energy distributions. The changes in laser power distribution that result from the three longhorn masks in this mask vector are likely more drastic than the real use cases. Therefore, this test mask provides an estimate of model accuracy using more difficult prediction cases. For the above mask vector, the MAPE remained within a range of 10–15%. While this indicates an increase from the ~5% MAPEs produced for single mask predictions, it shows that the surrogate model is robust to more complex inputs and sudden changes in laser exposure. Additional simulations and data extracted from a finer mesh resolution should improve this accuracy substantially for future model iterations. The percentage error for the results shown in Fig. 15 encompasses the full sintering domain, resulting in a conservative error percentage.

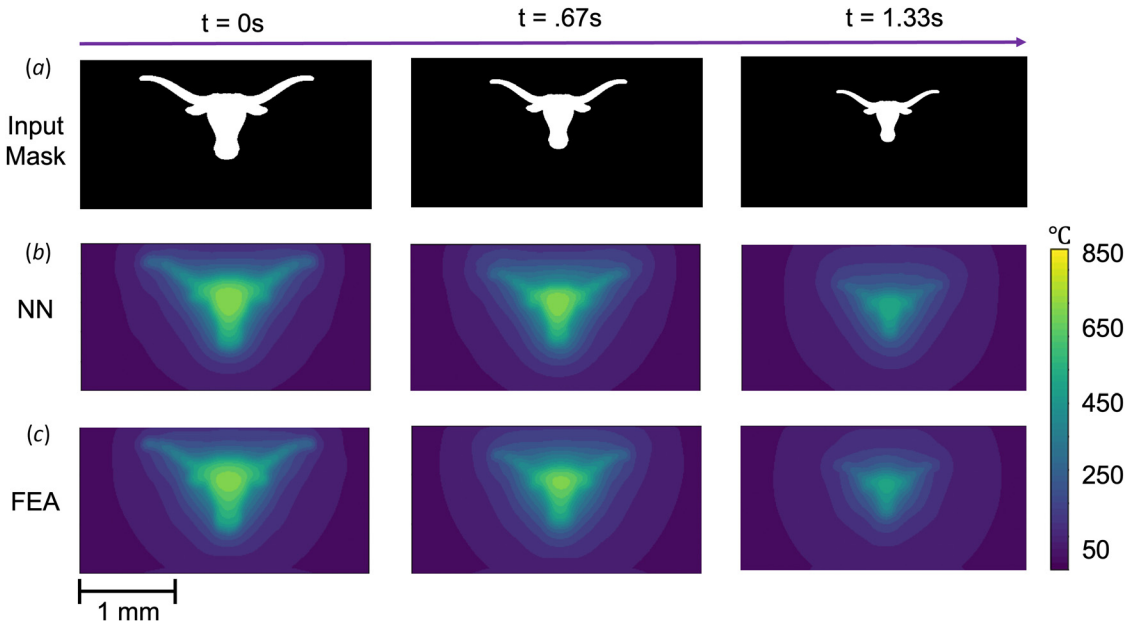

Fig. 15 Surrogate model results (top row) compared with FEA results (bottom row) for a single simulated sintering process over time using a variable mask vector. The images show the resulting temperature profiles after initial heating in response to the first mask, followed by the temperature profiles after each of the subsequent mask changes.

When the error percentage is restricted to exclude regions far from the laser source, the error range improves to 7–11%. This error will further improve with the addition of more robust training data and a more representative error metric. Additionally, mask changes used in real applications will likely be less drastic than those tested in this work, further reducing model error. Also, while it is likely possible to develop more accurate models using CNNs and graph neural networks, these models often more complex, and require many more simulations as input to the model. The model tested in this work required only nine simulations to produce accurate results.

Part Predictions. In addition to transient temperature predictions, the surrogate model also provides estimated sintered part shapes for a given sintering process. This is accomplished by incorporating the density-temperature property relationships developed in Refs. [19] and [20] into the surrogate modeling workflow. The surrogate model uses these property relationships to periodically update the density of each element to use as feature data for subsequent temperature predictions. These density values are stored each time they are updated during prediction, and can be used to visualize the regions of the sintering domain that have undergone substantial densification. The density prediction at the final timestep is used to estimate the shape of the final sintered part. These part estimates provide build predictions given the predicted temperature distribution in the particle bed. They also provide additional information regarding the accuracy of the print. A sample comparison of the sintered part shapes predicted by the NN surrogate model and the original FE model are shown in Fig. 16 along with the longhorn mask used as input to both models.

The predicted longhorn shapes show good agreement between the two models. Both models predict substantial sintering in the face of the longhorn, and minimal to nonexistent sintering near the horns. This is a direct result of the distribution of laser power in the powder bed, with the longhorn face experiencing the bulk of the laser exposure. The use of a nonuniform, optimized distribution of laser power for sintering of the longhorn shape will address the lack of sintering present in Fig. 16. Incorporating a higher laser power (brighter pixels) in the horn regions and darker pixels near the center of the exposure region will smooth out the temperature profile across the longhorn shape and improve the sintered part accuracy. The surrogate model prediction is somewhat asymmetrical when compared to the FE model prediction, but the overall size and shape show good agreement.

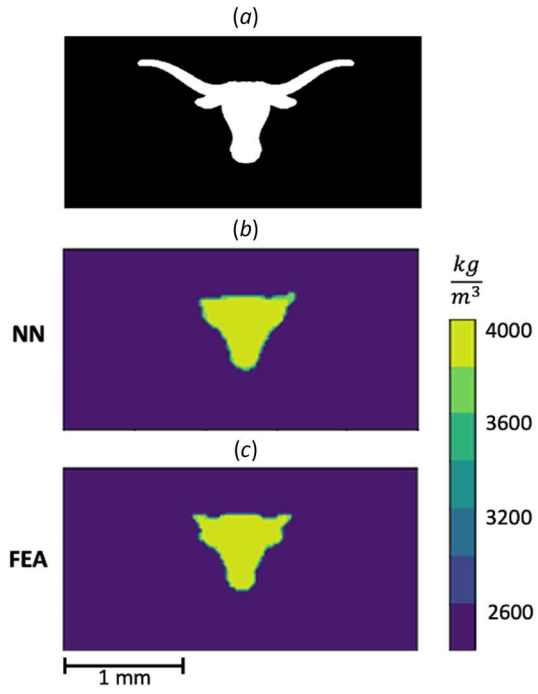

Fig. 16 Comparison of part density predictions from both the ANN and the FEA models. The longhorn mask was used as an input to both models.

Runtime Comparison. Despite the good agreement between the NN predictions and the FEA results, the NN predictions will always have additional error when compared to the FEA model. This small increase in error is offset by the greatly improved runtime of the NN. Currently, the NN predicts the full temperature timeseries in roughly 40 s, while the FE model takes roughly 30 min to fully solve for temperature. This equates to an approximate 45× increase in computational speed when using the NN as a temperature predictor. Given that the FE model is optimized for runtime and the NN is only partially optimized, there is room for improvement for the NN prediction speed. Additionally, the TensorFlow backend used to calculate the predicted temperatures scales exceptionally well for parallel predictions of element temperature. As a result, the NN prediction time will scale much more efficiently with a finer mesh grid when compared to the FE model. Once the FE model is refined, the speed increase when using the NN as a temperature predictor should be much greater than 45×. Additionally, the NN only requires three simulations for training to achieve good accuracy and fast computation times on single masks, and only nine simulations when predicting mask vectors, albeit at the cost of some accuracy. While this training dataset will be expanded to train the final version of the NN, this work presents a method to train an accurate finite element surrogate model on minimal training data. This helps to minimize the computational resources required to generate new models in response to changes in the parent FE model.

Model Validation and Future Work. The results presented in this work show good agreement between FEA and NN temperature predictions for both constant and variable laser power distributions. Laser power estimates were determined through preliminary calibration efforts using sintered copper layers. The laser powers used in this study are slightly higher than those used by the μ-SLS machine. The training framework outlined in this work was retrained using laser powers equaling 60% of the laser power used to develop the discussed results, and the prediction accuracy was nearly identical. These power values were chosen to test the trained models on a wider range of possible laser powers. This work introduces a model training framework where the NN is approximately learning the heat transfer process in a copper particle bed. This framework should be robust to changes in the underlying FEA model as long as the NN is retrained on the modified data.

The FE model has undergone preliminary validation with copper sintering experiments using the μ-SLS machine. Using a 1 mm × 1 mm square laser exposure region (controlled by a square-shaped binary mask), bed-scale FE model predictions were compared to physical parts sintered with the μ-SLS system. This sintering simulation was performed with the same mask for three different laser powers. The part shapes, along with their simulated counterparts, are shown in Fig. 17.

Part shapes predicted by the FE model agree with initial sintering experiments using copper nanoparticle inks. At 935 W, the sintered and simulated parts are very similar in shape and size, with corner curvature representing the major source of error in the prediction. This remains true for the 810 W comparison. For the lowest laser power of 560 W, the μ-SLS system produces a small square part, while the simulation does not predict part formation. While there appears to be a substantial discrepancy between the sintered part and the predicted part, analysis of the simulated temperatures reveals that the FE model predicted a max temperature of 442 °C. In other words, the FE model predicted a particle-bed just before the onset of sintering, while the real system produced a weakly sintered part. This likely results from an initial sintering process that initiates at temperatures below the 450 °C sintering threshold. Incorporating a

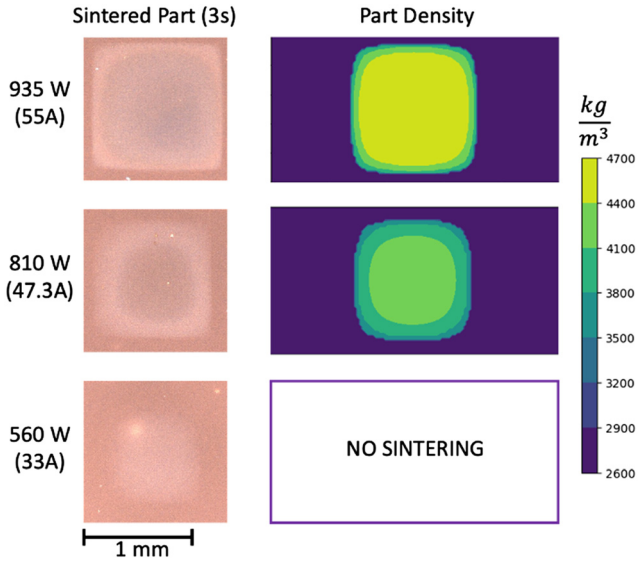

Fig. 17 Comparisons between part shapes sintered using the μ-SLS system and FE predicted part shapes for three laser powers (935 W, 810 W, 560 W)

ramping sintering model beginning at 400–425 °C instead of using a single sintering threshold will likely address this discrepancy. Further experimental validation of the FE model will help align the NN predictions with the μ-SLS system, but this validation process should not have a significant impact on the NN prediction accuracy. The NN model was trained on a separate set of simulated data with modified laser powers and energy distributions. Subsequent NN model testing produced results with very similar accuracy scores when compared to the original results. This paper proposes a general framework for sintering prediction for a μ-SLS system, using features that describe the heat flow conditions surrounding each element. Changes in the underlying FE model in response to extensive model validation will require generating a new training dataset, but the underlying heat flow features will continue to apply to the new system.

Conclusion

This work develops a regression-based surrogate model to enable rapid temperature predictions for the μ-SLS sintering process. This model is trained on data generated from a high-fidelity FE model to learn the heat transfer characteristics of a nanoparticle bed exposed to selective laser power. The surrogate model is capable of predicting the full timeseries evolution of temperature within the powder bed over a 2 s window with very good accuracy. The NN predictions on average achieve a 5.5% MAPE for the seven individual test masks used for comparison. The NN predictions on the complex mask vector achieved a MAPE ranging from 7% to 11% over the course of the simulation when estimating error near the region of interest. The NN predictions capture the thermal response to sudden changes in density and thermal conductivity that allow the FE model to account for thermal property evolution during sintering. This property evolution can then be used to predict the shapes of sintered parts. Although the FE model used to generate the data is inherently more accurate, the surrogate model runs more than 45× faster. This computational advantage will become more substantial as the mesh becomes finer during mesh refinement. This surrogate model enables the rapid timeseries predictions needed for parameter optimizations of the μ-SLS system. The model accuracy and performance will continue to improve through feature adjustments, further hyperparameter tuning, and an expansion of the training dataset.

Acknowledgment

The paper was presented at the 2023 Manufacturing Science and Engineering Conference (MSEC2023).

Funding Data

- This work was supported by NSF Grant No. 2141044; Funder ID: 10.13039/100000001.

Data Availability Statement

The datasets generated and supporting the findings of this article are obtainable from the corresponding author upon reasonable request.

Nomenclature

d = distance between elements in the mesh
Q_{gen} = heat generation experienced by an individual element
Q_{gen} Distance = feature summarizing spatial distribution of laser power though summation of $\frac{Q_{\text{gen}}}{d}$ ratio for all elements
Q_{gen} Zone = a ring-shaped region surrounding an element that details laser exposure

References

[1] Govett, T., Kim, K., Lundin, M., and Pinero, D., 2012, "Design Rules for Selective Laser Sintering," *Mechanical Engineering Design Projects Program*, The University of Texas, Austin, TX.
[2] Sager, B., and Rosen, D., 2002, "*Stereolithography Process Resolution*," Georgia Institute of Technology, Atlanta, GA.
[3] Roy, N. K., Behera, D., Dibua, O. G., Foong, C. S., and Cullinan, M. A., 2019, "A Novel Microscale Selective Laser Sintering (μ-SLS) Process for the Fabrication of Microelectronic Parts," Microsyst. Nanoeng., **5**(1), p. 64.
[4] Roy, N. K., Foong, C. S., and Cullinan, M. A., 2016, "Design of a Micro-Scale Selective Laser Sintering System," Proceedings of the 27th Annual International Solid Freeform Fabrication Symposium, Austin, TX, Aug. 8–10, pp. 1495–1508.
[5] Roy, N., Yuksel, A., and Cullinan, M., 2016, "Design and Modeling of a Microscale Selective Laser Sintering System," ASME Paper No. MSEC2016-8569.
[6] Roy, N., Dibua, O., Foong, C. S., and Cullinan, M., 2017, "Preliminary Results on the Fabrication of Interconnect Structures Using Microscale Selective Laser Sintering," ASME Paper No. IPACK2017-74173.
[7] Nelson, C., McAlea, K., and Gray, D., 1995, "Improvements in SLS Part Accuracy," Proceedings of the 1995 Annual International Solid Freeform Fabrication Symposium, Austin, TX, Aug., pp. 159–169.
[8] Grose, J., Liao, A., Tasnim, F., Foong, C. S., and Cullinan, M. A., 2023, "Part Scale Simulation of Heat Affected Zones for Parameter Optimization in a Microscale Selective Laser Sintering System," Proceedings of the 34th Annual International Solid Freeform Fabrication Symposium, Austin, TX, Aug. 14–16, pp. 847–862.
[9] Buffington, T., Bilyaz, S., and Ezekoye, O. A., 2021, "Brain-STORM: A Deep Learning Model for Computationally Fast Transient High-Rise Fire Simulations," Fire Saf. J., **125**, p. 103443.
[10] Tapia, G., Khairallah, S., Matthews, M., King, W. E., and Elwany, A., 2018, "Gaussian Process-Based Surrogate Modeling Framework for Process Planning in Laser Powder-Bed Fusion Additive Manufacturing of 316 L Stainless Steel," Int. J. Adv. Manuf. Technol., **94**(9–12), pp. 3591–3603.
[11] Kudela, J., and Matousek, R., 2022, "Recent Advances and Applications of Surrogate Models for Finite Element Method Computations: A Review," Soft Comput., **26**(24), pp. 13709–13733.
[12] Phellan, R., Hachem, B., Clin, J., Mac-Thiong, J. M., and Duong, L., 2021, "Real-Time Biomechanics Using the Finite Element Method and Machine Learning: Review and Perspective," Med. Phys., **48**(1), pp. 7–18.
[13] Liang, L., Liu, M., Martin, C., and Sun, W., 2018, "A Machine Learning Approach as a Surrogate of Finite Element Analysis-Based Inverse Method to Estimate the Zero-Pressure Geometry of Human Thoracic Aorta," Int. J. Numer. Methods Biomed. Eng., **34**(8), p. e3103.
[14] Vurtur Badarinath, P., Chierichetti, M., and Davoudi Kakhki, F., 2021, "A Machine Learning Approach as a Surrogate for a Finite Element Analysis: Status of Research and Application to One Dimensional Systems," Sensors, **21**(5), p. 1654.
[15] Masood, Z., Khan, S., and Qian, L., 2021, "Machine Learning-Based Surrogate Model for Accelerating Simulation-Driven Optimisation of Hydropower Kaplan Turbine," Renewable Energy, **173**(4), pp. 827–848.
[16] Dupuis, R., Jouhaud, J. C., and Sagaut, P., 2018, "Surrogate Modeling of Aerodynamic Simulations for Multiple Operating Conditions Using Machine Learning," AIAA J., **56**(9), pp. 3622–3635.

[17] Sikirica, A., Grbčić, L., and Kranjčević, L., 2023, "Machine Learning Based Surrogate Models for Microchannel Heat Sink Optimization," Appl. Therm. Eng., **222**, p. 119917.
[18] Greve, L., and van de Weg, B. P., 2022, "Surrogate Modeling of Parametrized Finite Element Simulations With Varying Mesh Topology Using Recurrent Neural Networks," Array, **14**, p. 100137.
[19] Vohra, M., Nath, P., Mahadevan, S., and Tina Lee, Y. T., 2020, "Fast Surrogate Modeling Using Dimensionality Reduction in Model Inputs and Field Output: Application to Additive Manufacturing," Reliab. Eng. Syst. Saf., **201**(2), p. 106986.
[20] Wang, Z., Jiang, C., Liu, P., and Yang, W., 2020, "Uncertainty Quantification and Reduction in Metal Additive Manufacturing," Npj Comput. Mater., **6**(1), p. 175.
[21] Zhao, X., Gong, Z., Zhang, J., Yao, W., and Chen, X., 2021, "A Surrogate Model With Data Augmentation and Deep Transfer Learning for Temperature Field Prediction of Heat Source Layout," Struct. Multidiscip. Optim., **64**(4), pp. 2287–2306.
[22] Chen, X., Chen, X., Zhou, W., Zhang, J., and Yao, W., 2020, "The Heat Source Layout Optimization Using Deep Learning Surrogate Modeling," Struct. Multidiscip. Optim., **62**(6), pp. 3127–3148.
[23] Yang, S., Yao, W., Zhu, L. F., and Ke, L. L., 2023, "Predicting the Temperature Field of Composite Materials Under a Heat Source Using Deep Learning," Compos. Struct., **321**, p. 117320.
[24] Hemmasian, A., Ogoke, F., Akbari, P., Malen, J., Beuth, J., and Farimani, A. B., "Surrogate Modeling of Melt Pool Thermal Field using Deep Learning," Additive Manufacturing Letters, 5, p. 100123.
[25] Pfaff, T., Fortunato, M., Sanchez-Gonzalez, A., and Battaglia, P. W., 2020, "Learning Mesh-Based Simulation With Graph Networks," International Conference on Learning Representations, Vol. 8, Apr. 26.
[26] Dibua, O. G., Yuksel, A., Roy, N. K., Foong, C. S., and Cullinan, M., 2018, "Nanoparticle Sintering Model, Simulation and Calibration Against Experimental Data," ASME Paper No. MSEC2018-6383.
[27] Grose, J., Dibua, O. G., Behera, D., Foong, C. S., and Cullinan, M., 2023, "Simulation and Property Characterization of Nanoparticle Thermal Conductivity for a Microscale Selective Laser Sintering System," ASME J. Heat Mass Transfer-Trans. ASME, **145**(5), p. 052501.